ACS OMEGA

Article

Cite This: ACS Omega 2017, 2, 6926-6938

http://pubs.acs.org/journal/acsodf

Solar-Light-Driven Improved Photocatalytic Performance of Hierarchical $ZnIn_2S_4$ Architectures

Sangeeta Adhikari,*,† Archana VijayKumar Charanpahari,† and Giridhar Madras

Department of Chemical Engineering, Indian Institute of Science, Bangalore 560012, Karnataka, India

ABSTRACT: In the quest for developing novel narrow band gap semiconductor materials, the research in metal chalcogenides has gained a strong attraction. In the present investigation, a surfactant-free hydrothermal route has been followed to design hierarchical self-assembled flower-like $ZnIn_2S_4$ structures through control over precursor concentration and hydrothermal processing parameters. Uniform hexagonal marigold flower-like $ZnIn_2S_4$ architectures (~4 μm) were formed with self-assembly of petals (thickness ~8−12 nm) forming rose-like structures and finally forming marigold flowers in 24 h duration. The hierarchical $ZnIn_2S_4$ flower structure has been used as photocatalysts for the degradation of dye and chlorinated phenols. Photodegradation demonstrates that the high surface area from the porous flower architecture (~72 m^2/g) with an enhanced visible light absorption giving low band gap energy (2.15 eV) is responsible for higher photocatalytic performance. Complete degradation of the organic pollutants has been observed within 90 min in the presence of natural sunlight. To understand the participating reactive species contributing to degradation, scavenger studies were performed for deducing the plausible photocatalytic degradation pathways. This study might open new insights into the design of novel hierarchical structures.

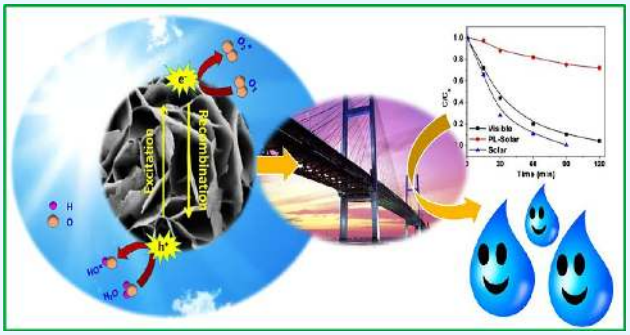

1. INTRODUCTION

Synthetic textile dyes constitute a large class of contaminated wastewater.[1,2] Azo- and fluorine-based dyes constitute a significant portion.[3,4] The degradation products of these dyes include aromatic amines that are highly carcinogenic. One of the widely used "green" technologies is heterogeneous photocatalytic oxidation processes for the decomposition of organic dyes soluble in wastewater.[5,6] Recently, attention has been paid to designing of new nontitania and nonoxides as effective materials that can harvest and show enhanced activity under visible light irradiation than under ultraviolet light.[7−10] Through these materials, the natural sunlight could be utilized more efficiently for the photocatalytic process. In a pursuit to develop such materials, self-assembled three-dimensional (3D) structures through one-dimensional and two-dimensional nanoscale building blocks have been used to form 3D hierarchical architectures.[11,12] Such hierarchical structures often lead to large surface area and open pore structures providing more active sites for favorable transport of electrons and holes to the surface for reaction to occur. Subsequently, this may lead to superior properties in comparison to the nanoscale materials.[13,14]

The ternary chalcogenide semiconducting compounds have acquired interest due to their tunable optical and electrical properties.[10,15] Among them, $ZnIn_2S_4$ has demonstrated potential applications in diverse fields such as thermoelectricity,[16] charge storage,[17] electrochemical recording, and as photocatalysis.[18−20] To achieve the optimum potentiality of the material, synthesis of $ZnIn_2S_4$ by various chemical methods plays a major role. The control of shape and size of these inorganic structures is of utmost importance because of the strong correlation between the synthesis parameters and physical/chemical properties.[21,22] Various researchers have reported the solution/soft chemistry route to be the best technique for synthesizing variant chalcogenide compounds with desired properties.[23,24]

Literature reports several different morphologies of $ZnIn_2S_4$ prepared via effective methods.[25] Shen et al. employed nanostructured $ZnIn_2S_4$ for hydrogen evolution, and the photocatalytic activity of $ZnIn_2S_4$ was greatly affected by the crystal plane spacing along the c axis.[11] One-dimensional $ZnIn_2S_4$ nanotubes and nanoribbons were synthesized by a solvothermal technique using pyridine as a solvent, and hollow microspheres were synthesized by the hydrothermal method using cetyl-trimethylammonium bromide or poly(ethylene glycol) surfactants.[26] In another study, porous polycarbonate membrane was used as a hard template to fabricate nanotubes and nanowires of $ZnIn_2S_4$, with the wall of the tubes 5 nm thick. $ZnIn_2S_4$ nanotubes imparted the highest visible light photoactivity for the degradation of methyl orange (MO) in 4 h.[27] Chen et al. studied the effect of $ZnIn_2S_4$ polymorphs for the degradation of rhodamine B and methyl orange, where the negative (0001) S plane enhanced the adsorption of cationic dyes over hexagonal $ZnIn_2S_4$ compared with methyl orange and

Received: September 8, 2017
Accepted: October 5, 2017
Published: October 20, 2017

DOI: 10.1021/acsomega.7b01329
ACS Omega 2017, 2, 6926−6938

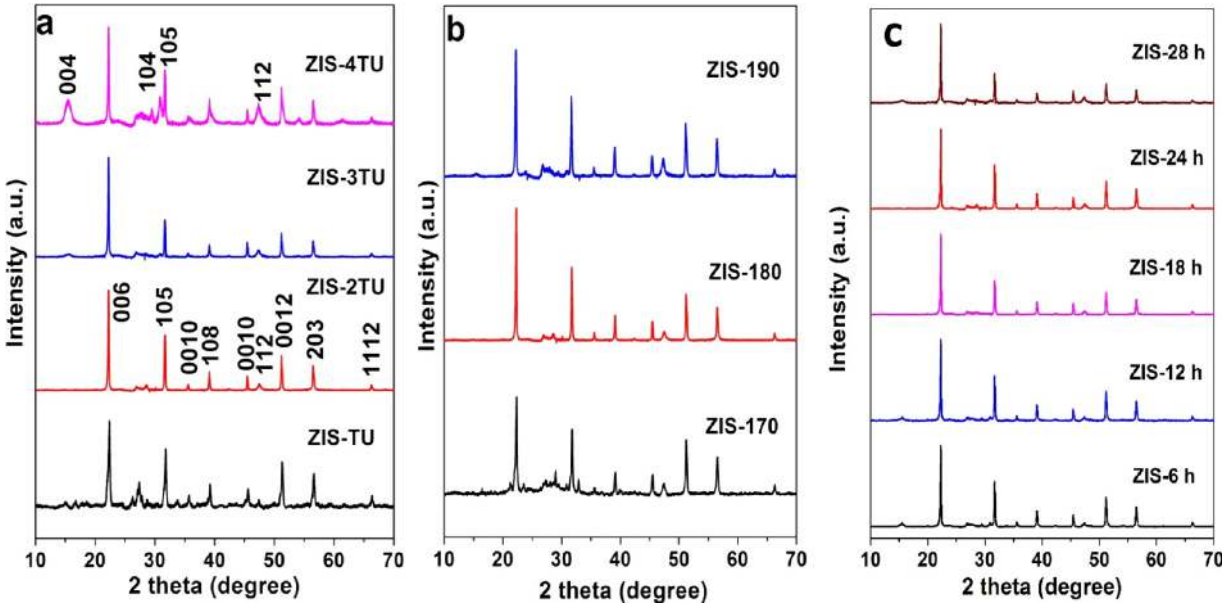

Figure 1. Composite XRD patterns as an effect of (a) thiourea content (parameters: temperature 180 °C and time 24 h); (b) hydrothermal temperature (parameters: thiourea content 2TU and time 24 h); and (c) hydrothermal duration (parameters: temperature 180 °C and thiourea content 2TU).

affects the photocatalytic activity synergistically.[28] Similar studies indicated rhodamine B is degraded by 97%, and only 5% methyl orange is degraded under the same conditions.[29] Most of the studies reveal the poor photocatalytic activity of $ZnIn_2S_4$ for the degradation of dyes.

Apart from the dye pollutants, chlorinated phenols are also contemporary in the system that results in high toxicity and serious environmental issues.[30,31] On the basis of the above context, development of a hierarchical material with well-defined structures and morphologies without surfactants and with enhanced surface activity to degrade these pollutants would be of great research interest. In the present study, we have reported the design and optimization of hierarchical $ZnIn_2S_4$ flower structures without any additional reagents. The concentration of precursor contents, hydrothermal temperature, and time have been varied to obtain a stable hierarchical structure. The optimized hierarchical $ZnIn_2S_4$ structure has been studied for the photocatalytic degradation of methyl orange. The degradation studies of chlorinated phenols were also carried out to understand the diversified effect of $ZnIn_2S_4$ structures.

2. RESULTS AND DISCUSSION

2.1. Effect of Processing Parameters on Crystal Structure. To investigate the purity of the crystal phase as an effect of different processing parameters such as thiourea content, hydrothermal temperature, and time, X-ray diffraction (XRD) measurements were carried out, and the results are represented in Figure 1a–c. Figure 1a presents the composite XRD pattern of the hydrothermally synthesized powders obtained with various stoichiometric contents of thiourea at a temperature of 180 °C for 24 h. The powders synthesized with stoichiometric thiourea are designated as ZIS-TU, whereas those with double the stoichiometric amount are designated as ZIS-2TU. Similarly, those with 3 and 4 times the stoichiometric thiourea are named as ZIS-3TU and ZIS-4TU, respectively. The XRD pattern of ZIS-TU shows a series of characteristic peaks, with a few peaks having low intensity. These peaks can be attributed to the hexagonal phase of $ZnIn_2S_4$ (JCPDS No. 72-0773).[32] However, it can be presumed that phase formation is not complete and yet to occur. It is clear from the figure that ZIS-TU has the lowest crystallinity in comparison to the other samples. When the thiourea content was doubled, sharp and high crystalline hexagonal peaks were prominent, with main characteristic peaks indexed to (006), (105), (0010), (108), (1010), (112), (0012), (203), and (1112) corresponding to the space group *P*63*mc* of hexagonal crystal structure. No other crystal phase related to the impurity phases such as binary sulfides and oxides are present, indicating the high phase purity of ZIS-2TU. With the higher content of thiourea (i.e., ZIS-3TU and ZIS-4TU), some of the crystal planes of hexagonal crystal phase are also observed to grow. A significant increment in hexagonal crystal planes (004), (104), (105), and (112) is observed to develop from ZIS-2TU to ZIS-3TU to ZIS-4TU. There were no traces of impurity peaks apart from the extra developed peaks that also correspond to the hexagonal crystal phase of $ZnIn_2S_4$. It is known that $ZnIn_2S_4$ exhibits different polytypes depending on the difference in stacking fashion of sulfur atoms in the matrix.[33] The coordination environment of ions in the solution governs the formation of either the hexagonal or cubic phase.[34] In the precursor solution, thiourea can form three different complexes with In^{3+} and Zn^{2+}, namely tetrahedral $[In(TU)_4]^{3+}$, $[Zn(TU)_4]^{2+}$, and octahedral $[In(TU)_6]^{3+}$. Under the hydrothermal conditions, the complexes $[In(TU)_6]^{3+}$ and $[In(TU)_4]^{3+}$ formed initially undergo Ostwald ripening and further react in situ with $[Zn(TU)_4]^{2+}$ to produce a thermodynamically stable hexagonal $ZnIn_2S_4$ containing both octahedral and tetrahedral coordination of In^{3+} ions.[35] Scherrer's formula was used to calculate the crystallite sizes of the synthesized powders. The calculated crystallite sizes are ~43, ~66, ~72, and ~72 nm for ZIS-TU, ZIS-2TU, ZIS-3TU, and ZIS-4TU, respectively. There is not much difference between the crystallite sizes of ZIS-2TU and ZIS-3TU, indicating that apart from the growth of few planes due to high thiourea content, it does not significantly affect the crystallite size. In this study, pure and stable hexagonal crystal

DOI: 10.1021/acsomega.7b01329
ACS Omega 2017, 2, 6926–6938

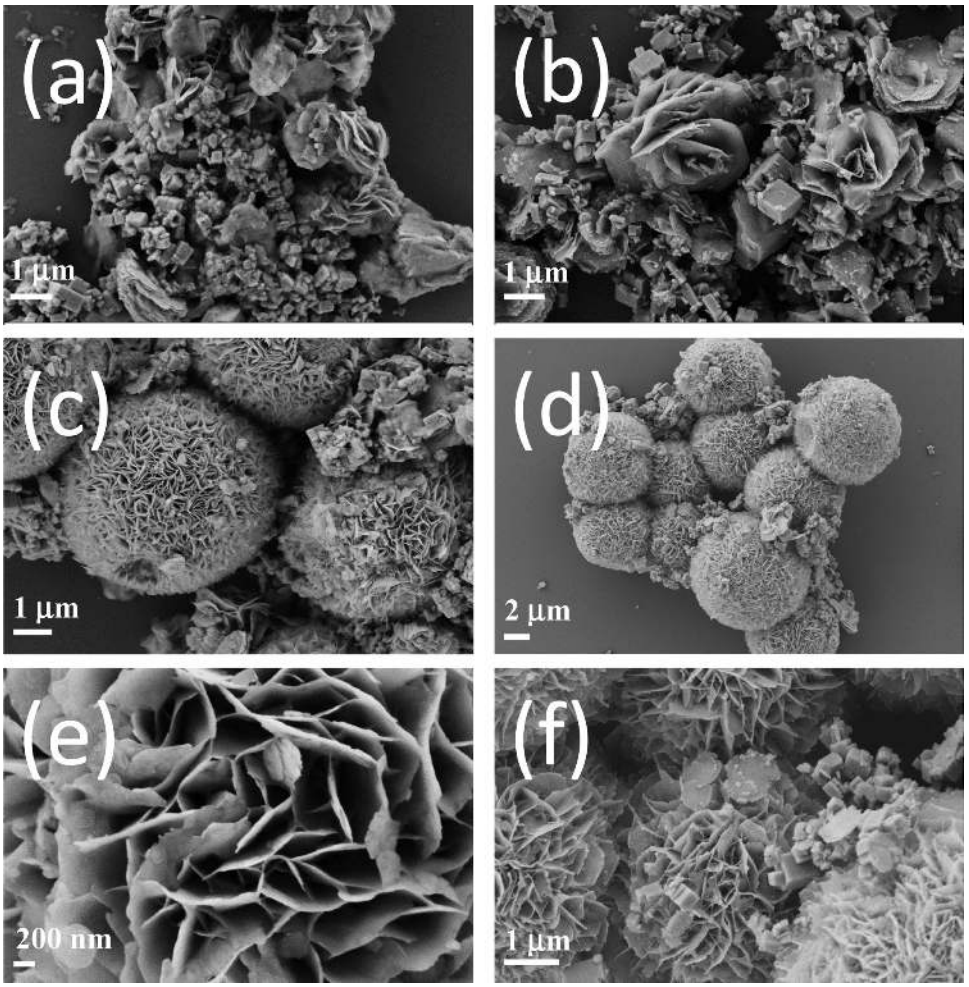

Figure 2. FESEM micrographs of powders synthesized at different hydrothermal duration (a) ZIS-6 h; (b) ZIS-12 h; (c) ZIS-18 h; (d, e) ZIS-24 h; and (f) ZIS-28 h.

phase of $ZnIn_2S_4$ was obtained at twice the stoichiometric amount of thiourea (ZIS-2TU). Thus, experiments for further process optimization were carried out keeping this amount thiourea content.

Figure 1b presents the XRD pattern of hydrothermal experiments performed with double the stoichiometric content of thiourea at different hydrothermal temperatures (170, 180, and 190 °C) kept for 24 h duration. The obtained powders were designated as ZIS-170, ZIS-180, and ZIS-190 for different temperatures. It can be observed that at 170 °C, some of the hexagonal peaks are still to be developed and become highly crystalline. Upon comparing the XRD pattern obtained for 170 and 180 °C, the peaks for ZIS-180 are highly crystalline compared with ZIS-170. This has also been confirmed from the calculation of crystallite sizes, which is ∼44 nm for ZIS-170, which is similar to that for ZIS-TU obtained in our previous XRD study. There is a sharp increase in the crystallite size from ∼66 to ∼110 nm (ZIS-190) when the temperature is raised from 180 to 190 °C. The crystallite size almost doubles probably due to Ostwald ripening of the particles at a high reaction temperature.[36] Thus, the particles synthesized at 180 °C is found suitable to form a highly crystalline stable and lower crystallite size hexagonal $ZnIn_2S_4$.

To identify the influence of hydrothermal duration on the crystal phase formation, identical set of experiments were performed at different time durations for 6, 12, 18, 24, and 28 h under the constant temperature of 180 °C and twice the stoichiometric amount of thiourea content in the precursor solution. The powders obtained were designated as ZIS-6 h, ZIS-12 h, ZIS-18 h, ZIS-24 h, and ZIS-28 h, as shown in Figure 1c. There was no significant change in the crystal phase of $ZnIn_2S_4$ synthesized at 6 and 28 h. However, an increment in the crystallite size is observed from ZIS-6 h (∼61 nm) to ZIS-28 h (∼74 nm). It was difficult to conclude the optimum time due to similar hexagonal crystal phases, thus microscopic imaging of these synthesized powders was carried out for optimization on the basis of morphology formation.

2.2. Morphological Analysis. A better understanding of the particle growth can be obtained from the microscopic imaging of the synthesized powders at different time intervals; thus, the powders were investigated by the field emission scanning electron microscopy (FESEM) technique. Figure 2a–f shows the images of the powders named ZIS-6 h, ZIS-12 h, ZIS-18 h, ZIS-24 h, and ZIS-28 h. A high agglomeration among particles with nonuniform shapes was observed for powders of ZIS-6 h (Figure 2a). Apart from these nonuniform particles, the presence of also plate-shaped particles indicates the development of some specific morphology. Upon increasing the hydrothermal duration to 12 h (Figure 2b), self-assembly of petal-like structures was observed to form rose-like structures along with other particles that are nonuniformly distributed in the system. However, further increasing the hydrothermal

DOI: 10.1021/acsomega.7b01329
ACS Omega 2017, 2, 6926−6938

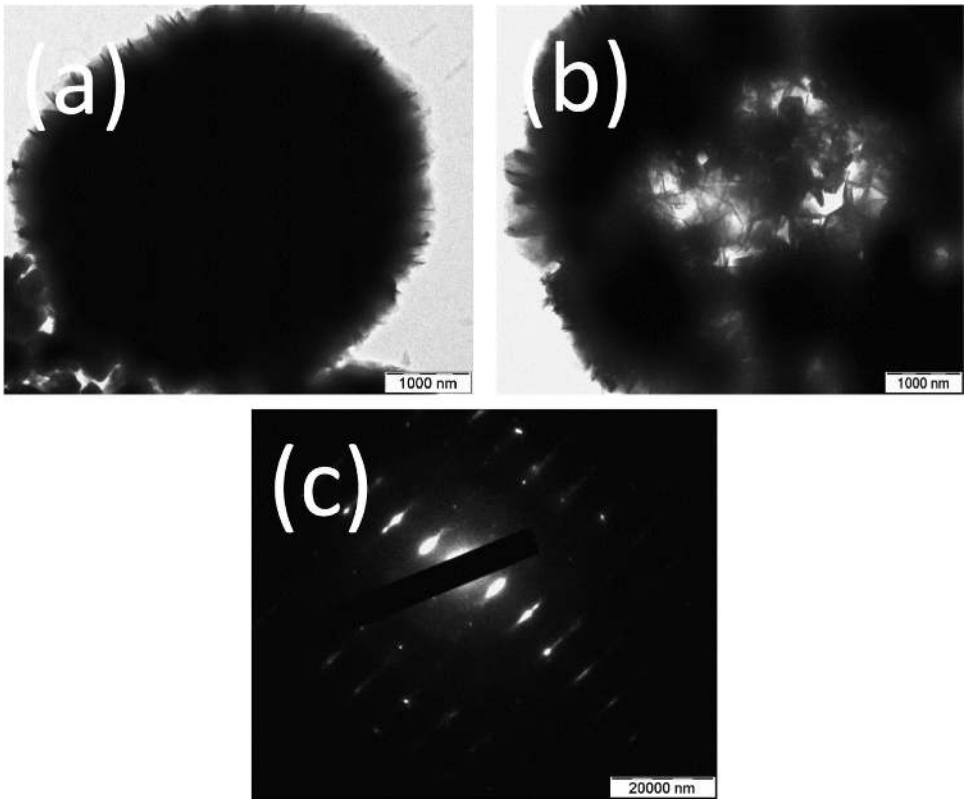

Figure 3. (a, b) TEM micrographs and (c) SAED pattern of ZIS-24 h.

duration to 18 h results in hierarchically spherical flower-like structures having an average flower size ∼3−5 μm (Figure 2c). There are also some petals over the surface of the flowers that are softly agglomerated and self-assembled to form flower-like structures. A careful observation reveals that the powder synthesized at 24 h duration has uniform spherical marigold flower-like structures that are well formed from the organization of petal structures. The average size of the flower is observed to be in the range of ∼4−7 μm (Figure 2d), which is higher than the flower size for ZIS-18 h. An area of the spherical marigold flower ZIS-24 h has been zoomed in to determine the thickness of the petals forming these structures as shown in Figure 2e. The thickness of the petals ranges from ∼8 to 12 nm. Further increasing the hydrothermal duration to 28 h shows an increment in these flower sizes varying from ∼7 to 10 μm (Figure 2f), which could be attributed to the growth of the flowers via Ostwald ripening process.[37] In both parts, Figure 2c,d, we observe an opening mouth, which is indicative of the hollow flower structures based on the high-resolution images shown later. The enhancement in the aspect ratio of the flower can be due to the lower petal thickness and self-assembly. The hierarchical marigold flower structure was observed to have open cavity size of ∼500 nm. It can be predicted that beyond 24 h, flowers merely grow to form flowers of enlarged size. The specific Brunauer−Emmett−Teller (BET) surface areas of ZIS-6 h, ZIS-12 h, ZIS-18 h, ZIS-24 h, and ZIS-28 h are 23, 24, 47, 72, and 62 m^2/g, respectively. It is quite evident that the surface area decreased after 24 h, which reveals that an increment in the flower size decreases the cavity distance between the petals, reducing the N_2 adsorption during the surface area measurement. A more detailed morphological and structural analysis for ZIS-24 h has been carried out as a part of optimized powder characterization.

Figure 3 shows the high-resolution transmission electron microscopy (TEM) image and selected area electron diffraction (SAED) pattern of powder synthesized at 24 h. Figure 3a,b shows two distinct natures of the same flower morphology. Some of the spherical flowers are opaque; however, some flowers are hollow, which was also observed in FESEM images mentioned previously. The average flower size has been observed to be ∼4 μm from Figure 3a. Formation of these hierarchical structures in aqueous media without any surfactant under hydrothermal conditions is possible by geometrical building blocks forming an array of particles that get layer curvatures and develop into flower structures as reported by Kale et al.[25] On the other hand, the development of hollow flower structures could be due to the assembly of small flowers to form a bigger flower, leaving behind a cavity in between the assembly. The edges of the flower are observed to be transparent. The selected area electron diffraction (SAED) pattern taken from the flower edge shows a distinct array of spots demonstrating the single crystalline nature of the $ZnIn_2S_4$ petals (Figure 3c). The advantage of this unique type of hierarchical marigold flower structures is that they impart a higher surface area due to open access to the interspaces between the interweaved petals that boosts the light-harvesting ability of the hierarchical structures through the multireflection process on the incident visible light and provides more active sites for the photocatalytic reaction.

2.3. Optical Properties. The optical properties of the $ZnIn_2S_4$ powders synthesized under different hydrothermal duration were investigated through UV−vis diffuse reflectance spectra. The reflectance data were converted to the Kubelka−Munk unit of absorption by means of Kubelka−Munk function,[35,38] and a plot of $F(R)^2$ versus photon energy is plotted (Figure 4a). The intersection of the extrapolated linear

DOI: 10.1021/acsomega.7b01329
ACS Omega 2017, 2, 6926−6938

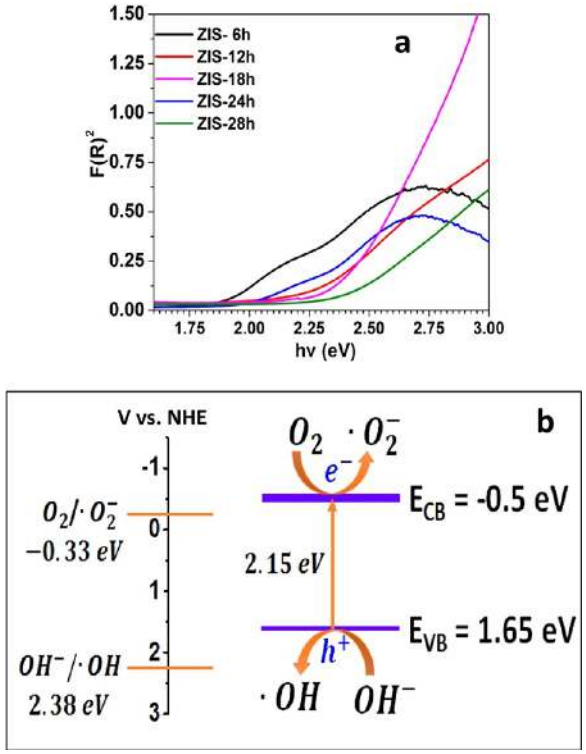

Figure 4. (a) Plot of the $F(R)^2$ vs photon energy for band gap determination and (b) calculated band positions of $ZnIn_2S_4$ and a possible mechanism for visible light photocatalysis.

portion to photon energy gives the estimation of band gap energy values (E_g). The E_g values varied with respect to hydrothermal duration and range from ∼1.77 to 2.49 eV. The E_g value for ZIS-24 h is estimated to be 2.15 eV, which is similar to the reported band gap values for $ZnIn_2S_4$ structures.[21,39,40] Furthermore, the conduction and valence band positions of the optimized $ZnIn_2S_4$ flowers were determined from the estimated band gap values using the following equation[41]

$$E_{VB} = X - E_e + 0.5E_g \quad (1)$$

where E_{VB} and E_{CB} are valence band and conduction band edge potentials, E_e is the energy of free electrons on the hydrogen scale (4.5 eV), E_g is the band gap energy, and X is the electronegativity of the semiconductor. The estimated valence band edge potential is 1.65 eV, and the corresponding conduction band edge potential is estimated to be −0.5 eV. On the basis of the calculated band positions, the possible mechanism for visible light photocatalysis over $ZnIn_2S_4$ flower structures is shown in Figure 4b. It can be well observed that the valence band of $ZnIn_2S_4$ is less positive than that of E° ($^\bullet OH/OH^-$) (1.65 V vs normal hydrogen electrode (NHE)), indicating that the photogenerated holes are not able to oxidize OH^- to give $^\bullet OH$.[28] The conduction band is more negative than E° ($O_2/O_2^{-\bullet}$) (−0.33 V vs NHE), indicating that the photogenerated electrons can reduce the surface chemisorbed O_2 to yield the strong oxidizing species $O_2^{-\bullet}$. From the above observation, it could be presumed that the photocatalytic reaction via $ZnIn_2S_4$ is favorable through photogenerated electron converting the adsorbed oxygen molecules on the surface of the flower to superoxide radical as an active species. To validate this hypothesis, photocatalytic reaction in the presence of different scavengers were performed, as discussed in the later section.

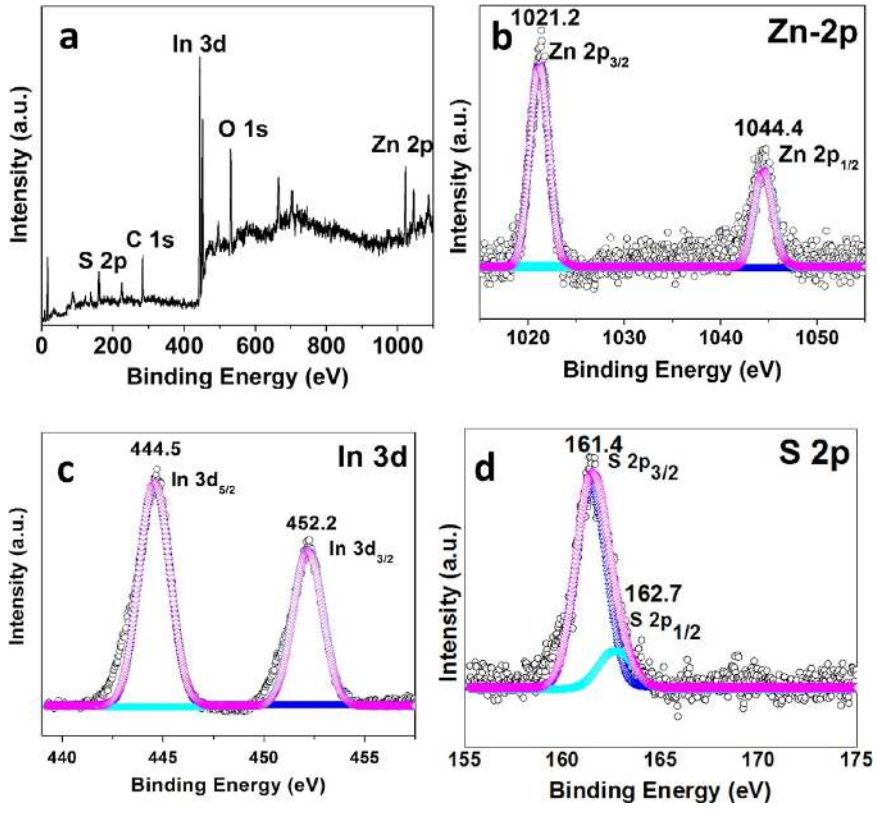

Figure 5. (a) Wide survey; (b) Zn-2p core level; (c) In-3d core level; and (d) S-2p core level XPS spectra of $ZnIn_2S_4$ flower structures.

DOI: 10.1021/acsomega.7b01329
ACS Omega 2017, 2, 6926−6938

2.4. Compositional Analysis. A significant investigation on the surface chemical states of the synthesized $ZnIn_2S_4$ flower using the X-ray photoelectron spectroscopy (XPS) measurement is essential, as the trace content of any impurity that cannot be detected in other analytical methods can have a synergistic influence over the photocatalytic properties of the material. Figure 5 shows the wide survey of $ZnIn_2S_4$ and the corresponding elements Zn-2p, In-3d, and S-2p. The wide survey scan clearly shows the specific peaks for the presence of elements C, O, Zn, In, and S (Figure 5a). The binding energy for the C-1s peak at 284.6 eV was used as the reference for calibration, as it is attributed to the adventitious carbon species on the samples. The peaks in Zn, In, and S elements were deconvoluted to identify any trace impurities. The binding energies centered at 1021.2 and 1044.4 eV of Zn-2p (Figure 5b) correspond to the Zn-$2p_{3/2}$ and Zn-$2p_{1/2}$, respectively, which governs Zn to be in the Zn^{2+} form in $ZnIn_2S_4$.[42,43] The binding energies at 444.5 and 452.2 eV in XPS spectra of In-3d can be well attributed to the In-$3d_{5/2}$ and In-$3d_{3/2}$, respectively (Figure 5c), indicating In^{3+} to be the existing form. The XPS spectra of S-2p were deconvoluted into two separate peaks centered at 161.4 and 162.7 eV, as shown in Figure 5d indexed to S-$2p_{3/2}$ and S-$2p_{1/2}$, respectively, confirming the S^{2-} form of sulfur.[44] The XPS signals obtained are consistent with the available literature values. The absence of any other elemental peaks and surface states other than C and O from atmospheric absorption confirms the chemical purity of the synthesized $ZnIn_2S_4$ flower structures.

2.5. Photocatalytic Studies. We optimized the hierarchical $ZnIn_2S_4$ flower structure synthesized at 180 °C for 24 h with a double thiourea content (ZIS-24 h) to be the photocatalyst that will be used for the investigation of degradation of a model pollutant, methyl orange (MO). Apart from the optimization of the photocatalyst through morphology, the photocatalytic tests were also performed for individual $ZnIn_2S_4$ samples prepared under different reaction parameters prior to the systematic photocatalysis using the optimized photocatalyst. A series of degradation experiments were carried out under metal halide lamp with each of the synthesized catalyst with catalyst loading of 50 mg/50 mL and the corresponding degradation results has been tabulated in Table 1. The results depict that each of the synthesized $ZnIn_2S_4$ particles show variation in the specific surface area due to the hydrothermal processing conditions governing the morphology formation, which indeed have a significant effect on the photocatalytic degradation of MO. Prior to each of the photocatalytic experiment, adsorption−desorption equilibrium was achieved without light irradiation, and the absorbance obtained after adsorption was considered as the initial concentration for the photocatalytic experiments. The highest photoactivity of 96% was achieved with ZIS-24 h, which also has a high specific surface area among other synthesized photocatalysts, proving the superiority of the ZIS-24 h powders. The results also provide insight into the morphology-driven photoactivity following a trend: ZIS-6 h (nonuniform/plate particles, 54%) > ZIS-12 h (rose-like structure, 67%) > ZIS-24 h (hierarchical flower structure, 96%). The degradation with ZIS-18 h and ZIS-28 h is lower, as the surface area of ZIS-18 h is low due to the presence of some agglomerated plates on the surface of hierarchical flower structure and the phenomenon of Ostwald ripening in ZIS-28 h reduces the surface area because of prolonged hydrothermal duration. Thus, based on the photocatalytic tests, the hierarchical $ZnIn_2S_4$ flower synthesized at 180 °C for 24 h with double thiourea has been optimized.

Table 1. Specific Surface Area and Photocatalytic Degradation Results of $ZnIn_2S_4$ Sample Series Synthesized Under Different Reaction Conditions

sample name	surface area (m^2/g)	% degradation
ZIS-3TU	46	75
ZIS-170	45	68
ZIS-190	54	79
ZIS-6 h	19	54
ZIS-12 h	24	67
ZIS-18 h	47	78
ZIS-24 h	72	96
ZIS-28 h	62	87

The surface charge of the photocatalysts plays an important role in the adsorption of dye pollutants. Although literature reports the surface charge of $ZnIn_2S_4$ to be negative,[29] confirmation of adsorption ability is much needed before detailed photocatalytic analysis. Therefore, prior to the systematic photocatalytic experiments, dye pollutant with contrary charges such as methylene blue (MB, a cationic dye) and methyl orange (MO, an anionic dye), which is the model pollutant in our case, was allowed to adsorb onto the $ZnIn_2S_4$ surface under dark conditions (50 mg catalyst/50 mL 20 ppm dye solution). We observed complete adsorption of MB on the $ZnIn_2S_4$ surface within 60 min, whereas only 22% MO adsorption takes place in 120 min, which remains constant afterward. The above results point toward the negative charge on the surface of flower-like $ZnIn_2S_4$ structures, which allows adsorption of the MB molecules on the surface of the catalyst. A similar result has been obtained by Chen et al.,[28] where they have reported that the exposed negative (0001) S plane of hexagonal $ZnIn_2S_4$ is responsible for the adsorption of cationic dye.

The variation in C/C_o of MO (where C is the concentration at time t and C_o is the initial concentration after adsorption equilibrium) as a function of time under different catalyst loading conditions is shown in Figure 6a. Before the initiation of catalytic experiments, the degradation of dye in the presence of visible light solely was carried out to understand the degradation in the presence of light and the observed photolytic degradation (PL) of MO was only 12%. Most of the studies have shown negligible adsorption of MO; however, in the present case, adsorption of methyl orange over $ZnIn_2S_4$ was observed to be 14, 22, and 25% with catalyst loading of 25, 50, and 100 mg/50 mL 20 ppm MO, respectively, which increases with increase in the catalyst loading. This increased adsorption could be attributed to the open cavities in the flower structures of $ZnIn_2S_4$, which facilitate the adsorption of dye. However, there is no significant increment in adsorption with the doubling of catalyst loading from 50 mg (22%) to 100 mg (25%). After the adsorption equilibrium, the visible light was switched on to carry out the photocatalytic experiments. We observe that the degradation increased from 92 to 96% when the catalyst loading is doubled from 25 to 50 mg/50 mL for 20 ppm MO. However, further doubling the loading from 50 to 100 mg decreases the catalytic activity to 88%. This decrease in catalytic activity could be attributed to the increased agglomeration among particles due to higher loading content, which reduced the active sites due to agglomeration. Another reason is that absorption of light by the particles reduces due to

DOI: 10.1021/acsomega.7b01329
ACS Omega 2017, 2, 6926−6938

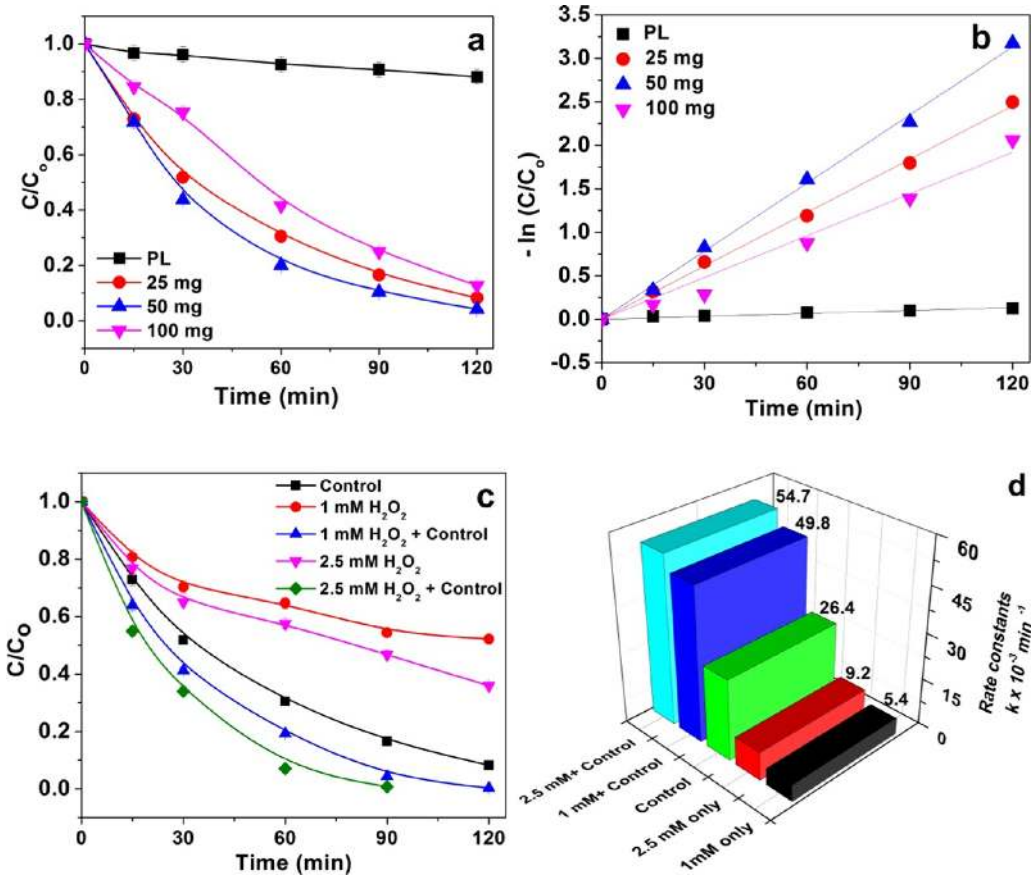

Figure 6. (a) Degradation profile; (b) kinetic profile (parameters constant: MO concentration 20 ppm, and temperature 25 ± 2 °C); (c) degradation profile with respect to oxidizer H_2O_2; and (d) first-order rate constant vs oxidizer concentration in control system.

segregation of particles and thus reduces the activity.[45] The photocatalytic activity is comparable for all of the loadings. Therefore, first-order kinetic plot of $-\ln C/C_o$ versus time was plotted to determine the kinetic rate constants with respect to catalyst loading, which would give insight into the choice of catalyst loading. Figure 6b presents the kinetic plot of photolysis and also loading effect on the photochemical reaction. The reaction follows the pseudo-first-order kinetics as shown in the figure. The kinetic rate constants with respect to different catalyst loading are 16.3, 26.4, and 17.2 ($\times 10^{-3}$) min^{-1} for 25, 50, and 100 mg/50 mL of 20 ppm MO, respectively. The above data suggest that the rate of the reaction is almost halved with an increase in catalyst loading to 100 mg and also with a decrease in catalyst loading to half. There is a 1.6-fold increase in the rate constants of 25 and 50 mg catalyst loadings. On the basis of the above findings, the highest photocatalytic degradation with the highest rate constant is observed with a catalyst loading of 50 mg and has been used for further photocatalytic experiments.

The presence of an oxidizer in the photochemical system acts as a booster for the production of reactive species and thus is an important additive for improving the photocatalytic activity of any material. Figure 6c shows the effect of the presence of the oxidizer H_2O_2 and its comparative photocatalytic degradation under the influence of visible light irradiation. The reactions carried out under different conditions are designated as follows: (a) in the presence of oxidizer H_2O_2 only, without a catalyst; (ii) in the presence of catalyst only, without H_2O_2, named as control; and (iii) in the presence of both H_2O_2 and catalyst. The concentration of hydrogen peroxide has been varied as 1 and 2.5 mM in the photochemical control reactions. The dye degradation in the presence of H_2O_2 under visible light irradiation is via photolysis of the oxidizer H_2O_2, which is through the hemolytic cleavage of H_2O_2 producing $HO^\bullet$ radicals that contribute to the photochemical reaction as shown in eq 2.[46] In addition, H_2O_2 is also capable of accepting the photogenerated electron from $ZnIn_2S_4$ that inhibits the electron−hole pair recombination and also facilitates additional $HO^\bullet$ radicals, as shown in eq 3

$$H_2O_2 \rightarrow 2HO^\bullet \quad (2)$$

$$H_2O_2 + e^- \rightarrow HO^\bullet + HO^- \quad (3)$$

The degradation observed in the presence of H_2O_2 having concentrations of 1 and 2.5 mM is 48 and 65%, respectively. This phenomenon indicates that the hydroxyl radical production for the degradation of MO in the presence of H_2O_2 is quite fast, and complete degradation of the dye can be achieved within less time. Comparing the photocatalytic degradation in the presence of H_2O_2 with control and control itself, complete degradation is achieved within 90 min in the presence of H_2O_2, where more than 90% degradation happens in the first hour. This suggests that increment in H_2O_2 concentration has a significant effect on the degradation and its presence greatly influences the photochemical system. Figure 6d presents the first-order rate constants of the photochemical reactions, which evidently indicate that the rate of the reaction increases significantly in the presence of 1 and 2.5 mM H_2O_2, which is 54.7 and 49.8 ($\times 10^{-3}$) min^{-1},

DOI: 10.1021/acsomega.7b01329
ACS Omega 2017, 2, 6926−6938

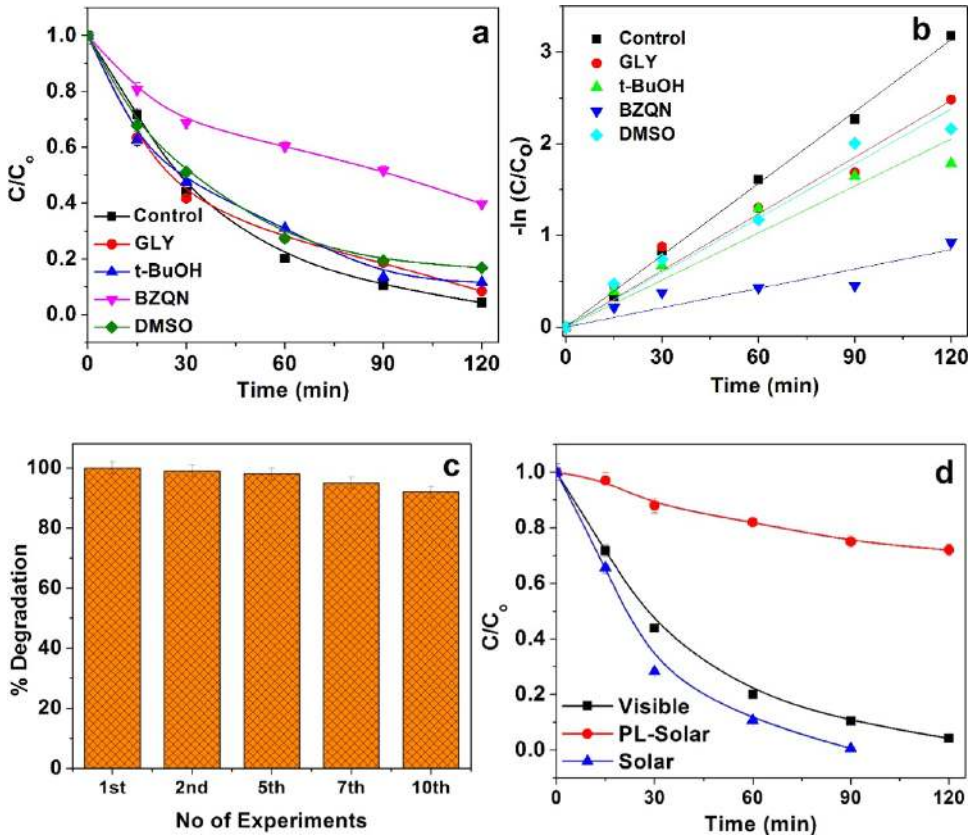

Figure 7. (a) Degradation profile; (b) kinetic profile of photochemical reaction carried in the presence of various scavengers (catalyst concentration 50 mg/50 mL 20 ppm MO, temperature 25 ± 2 °C, scavenger concentration 1 mM); (c) catalyst reusability studies; and (d) degradation profile for MO in the presence of natural sunlight (solar).

respectively. There is a 1.8 and 2.0 times increase in the rate constant in comparison to the control. The rate constant of control is higher than that of the reaction carried out with the oxidizer solely. It is well observed that complete photochemical degradation of MO also takes place in the presence of 1 mM H_2O_2. Because the photolytic degradation of MO in the presence of 1 mM H_2O_2 solely is also high, we presumed the degradation to happen much faster within less time. The above results suggest that there might be an ongoing competition between the oxidizer-produced hydroxyl radicals and other produced photoreactive species in the photochemical system for degradation of MO. To understand the reactive species active in degradation of MO, experiments were carried out in the presence of different reactive species scavengers without the presence of oxidizers.

As already predicted from the valence band and conduction band potential calculations in Section 2.3, the photocatalytic reaction via $ZnIn_2S_4$ is favorable through photogenerated electron converting the adsorbed oxygen molecules on the surface of the $ZnIn_2S_4$ to superoxide radical as an active species. Figure 7a shows the variation in C/C_o of MO as a function of irradiation time before and after the scavengers were added to the photochemical system. The prime role of these active species was determined through the variation in C/C_o of the dyes after the scavengers were introduced in the system. Only 57% of MO was degraded upon introducing benzoquinone (BZQN) to the photochemical system, and there was an obvious inhibition of the photochemical degradation. There was no significant suppression of the catalytic degradation with the addition of other scavengers such as *tert*-butyl alcohol (*t*-BuOH, $OH^•$ scavenger), glycerol (GLY, h^+ scavenger), and dimethyl sulfoxide (DMSO, e^- scavenger). It can be observed that with the addition of GLY, the concentration of MO decreased quickly in the first 60 min and then became slow. The results indicate that quite a large number of $O_2^{-•}$ were generated when the catalyst was irradiated with visible light, and this played an important role in the degradation of the dye. The dye degradation was slightly suppressed when DMSO was added to the system in comparison to *t*-BuOH. Under the visible light irradiation of $ZnIn_2S_4$ in the system, electrons in the valence band transfer to the conduction band and form electron−hole pairs. The photoexcited electrons also have the possibility of the recombination either at the surface or directly that may result in reduced efficiency. However, the recombination was obviously restrained when glycerol was added into the system to scavenge the holes. So, during this time, more electrons get migrated to the surface of the photocatalyst and react with O_2 to produce $O_2^{-•}$, enhancing the dye degradation initially. Figure 7b shows the first-order kinetic plot varying with time supporting the above observations. There is 3.4 times decrease in the rate constant when benzoquinone (7.7×10^{-3} min^{-1}) was introduced into the system in comparison to the control (26.4×10^{-3} min^{-1}). The photochemical reactions that follows during the degradation process are as follows

$$ZnIn_2S_4 + h\nu \rightarrow ZnIn_2S_4(h^+ + e^-) \quad (4)$$

$$O_2 + e^- \rightarrow {}^•O_2^- \quad (5)$$

DOI: 10.1021/acsomega.7b01329
ACS Omega 2017, 2, 6926−6938

$$^{\bullet}O_2^- + H^+ \rightarrow HO_2^{\bullet} \quad (6)$$

$$2HO_2^{\bullet} \rightarrow O_2 + H_2O_2 \quad (7)$$

$$H_2O_2 + {}^{\bullet}O_2^- \rightarrow {}^{\bullet}OH + OH^- + O_2 \quad (8)$$

$$H_2O_2 + h\nu \rightarrow 2{}^{\bullet}OH \quad (9)$$

The catalyst recyclability and stability is an important factor in heterogeneous catalysis. Thus, recyclability of the synthesized $ZnIn_2S_4$ catalyst has been carried out to understand the variation in the reactivity of the samples with consecutive reuse, till 10 cycles (Figure 7c). After each of the photochemical experiments, the catalyst was separated from the dye solution via centrifugation, washed with water and ethanol, followed by drying at 70 °C for 12 h in hot air oven. The dried catalyst was then reused for the second experiment consecutively. However, it can be noticed that the dye degradation decreased slightly with each consecutive recycle, suggesting that first run has the highest degradation efficiency, which decreases with the increasing number of reuse cycles. This decrease is due to the loss of catalyst during the process of recycling and also due to the blockage of active sites, resulting in less activity compared to the pristine powder. A difference of ∼9% after the 10th run indicates that the catalyst is stable and recyclable. The surface area of the catalyst before and after reuse was measured, and a difference of 7 m^2/g was observed. Thus, the above data confirm that the active surface site also decreases with decrease in the surface area; therefore, the photocatalytic activity drops in consecutive experimental runs.

$ZnIn_2S_4$ is a visible light active photocatalyst; thus, the experiments are also performed under natural solar light and compared with the above experiments to understand the difference in efficiency with reduced time interval. Figure 7d presents the comparative plot of C/C_o for the photocatalysis performed under natural sunlight (solar) and visible light. Similar to the previous experiments, photolysis of the dye was carried out under sunlight to understand the degradation of dye under the influence of sunlight. The photolysis of MO dye under sunlight was ∼22%. MO degradation under natural sunlight was 90% in the first 60 min, out of which 70% degradation happens in 30 min. On the other hand, degradation under visible light was only 55% in 30 min and 75% in 60 min. The complete degradation of 20 ppm MO was achieved within 90 min in the presence of natural sunlight without any oxidizer using hierarchical $ZnIn_2S_4$ flower structure. The probable reason behind complete degradation within less time could also be attributed to the 3−5% of UV light being constituted in the radial distribution of the natural sunlight. Comparison of the photocatalytic results of different $ZnIn_2S_4$ morphologies/structures with the present work (Table 2), it is promisingly efficient catalyst for visible light driven photocatalysis for the degradation of organic pollutants.

2.6. Photocatalytic Studies of Chlorinated Phenols. Chlorinated phenols are typical organic pollutants possessing serious threat to the water systems, as they are colorless pollutants and nonbiodegradable. The photocatalytic activity of the optimized hierarchical $ZnIn_2S_4$ flower structure has been investigated for the degradation of 2,4-dichlorophenol (2,4-DCP) and 2,4,6-trichlorophenol (2,4,6-TCP) under irradiation of natural sunlight. Figure 8a illustrates the degradation profile of 2,4-DCP and 2,4,6-TCP, respectively. To understand the possibility of degradation by sunlight irradiation, the blank experiment was carried out where the organic contaminants

Table 2. Comparison of Photocatalytic Performances in Other $ZnIn_2S_4$ Structures and This Work

$ZnIn_2S_4$ structures	synthesis route and chemicals	surface area (m^2/g)	pollutants concentration	light source	degradation in time	ref
$ZnIn_2S_4$ microspheres	hydrothermal and $ZnCl_2$, $InCl_3{\cdot}4H_2O$, C_2H_5NS	85.5	methyl orange 10 ppm, Congo red 20 ppm, rhodamine B 30 ppm	500 W W-halogen lamp	100% in 240 min, 100% in 300 min, 100% in 180 min	47
$ZnIn_2S_4$ nano/micropeony	solvothermal and CH_3OH, $Zn(NO_3)_2{\cdot}6H_2O$, $In(NO_3)_2{\cdot}5H_2O$, CS_2, CH_2Cl_2	78.2	methylene blue 50 ppm	300 W W-halogen lamp	100% in 90 min	37
$ZnIn_2S_4$ microspheres	solvothermal and $ZnSO_4{\cdot}7H_2O$, $InCl_3{\cdot}4H_2O$, CH_3CSNH_2, C_2H_5OH	86.2	benzyl alcohol	300 W Xe lamp	80% selectivity in 120 min	18
$ZnIn_2S_4$ nanoparticles	hydrothermal and $Zn(NO_3)_2{\cdot}6H_2O$, $In(NO_3)_2{\cdot}5H_2O$, C_2H_5NS		methyl orange 20 ppm	500 W W-halogen lamp	52% in 300 min	48
$ZnIn_2S_4$ flower-like microspheres	$ZnCl_2$, $InCl_3{\cdot}4H_2O$, C_2H_5NS				100% in 300 min	
hierarchical $ZnIn_2S_4$ flower structure	hydrothermal and $Zn(NO_3)_2{\cdot}6H_2O$, $In(NO_3)_2{\cdot}5H_2O$, CH_4N_2S	72	methyl orange 20 ppm, 2,4-dichlorophenol (2,4-DCP) 50 ppm, 2,4,6-trichlorophenol (2,4,6-TCP) 50 ppm	natural sunlight	100% in 90 min, 100% in 120 min, 100% in 75 min	this work

DOI: 10.1021/acsomega.7b01329
ACS Omega 2017, 2, 6926−6938

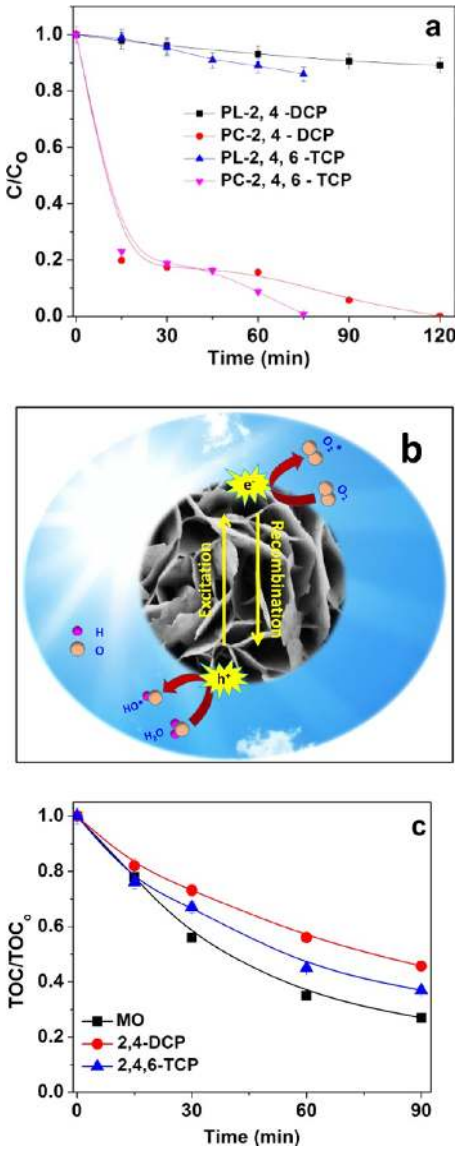

Figure 8. (a) Degradation profile of chlorinated phenols under natural sunlight; (b) schematic photocatalytic mechanism via hierarchical $ZnIn_2S_4$ flower structures; and (c) time-resolved total organic carbon (TOC) plot for MO, 2,4-DCP, and 2,4,6-TCP.

were degraded without any catalyst. The photolytic results suggests that the photosensitized self-decomposition of these colorless pollutants under the present experimental conditions is nearly 12 and 15% for 2,4-DCP and 2,4,6-TCP, respectively. Moreover, there is an appreciable adsorption of 60 and 38% of 2,4-DCP and 2,4,6-TCP on the catalyst surface. Similar to the experiments carried out for dye degradation, herealso, the absorbance values for adsorption are considered as the initial concentration of the chlorinated phenols. Almost 80% of the degradation takes place within 15 min, and then gradual complete degradation of the pollutant has been observed, where 2,4-DCP and 2,4,6-TCP is completely degraded within 120 and 75 min, respectively. The photodegradation of these nonbiodegradable colorless compounds has been found to be effective and faster in the presence of natural sunlight. The above results also suggest that the degradation becomes faster with increase in substitution.

A comparison of the degradation efficiencies of both the chlorinated phenols shows that the degradation of 2,4,6-trichlorophenol (2,4,6-TCP) was much faster than that of 2,4-dichlorophenol (2,4-DCP). These divergences in the same reaction could be due to the efficient attack at the chlorinated positions by reactive oxygen species and also due to no expected chain reaction of the generated chlorine radicals ($Cl^{\bullet}$) during the photochemical reaction. There is also a possibility of autocatalysis, which is a simultaneous attack from the $Cl^{\bullet}$ radical.[49−51] The above analysis indicates that the degradation of highly chlorinated phenol is more rapid and favorable than the less-chlorinated phenols because of the increase in the production of chloride ions. Consecutively, the as-synthesized $ZnIn_2S_4$ acts as a potential photocatalyst in the degradation of dye colorants and also phenolic systems for efficient remediation toward environmental contaminants.

It is quite usual to point out that the high surface area of hierarchical structures mainly contributes to the improvement in the photocatalytic activity, and the increase in photo-absorption due to the interspace between the petals also increases the efficiency of degradation. Another major advantage is the enhanced adsorption that enables the fast photocatalysis via superoxide radicals preventing the recombination of electron−hole due to proficient photochemical reactions, as shown in Figure 8b. All of these considerations suggest that the as-synthesized hierarchical $ZnIn_2S_4$ flower structures are potentially useful photocatalysts for many versatile organic pollutants.

The photochemical degradation reaction can undergo both decolorization and mineralization processes. To further confirm these occurrences, the total organic carbon (TOC) content in the solution taken at regular intervals was evaluated for both the dye and chlorinated phenols. The TOC/TOC_o values are plotted against solar irradiation time and have been shown in Figure 8c. It can be observed that the total organic carbon decreased nearly 70, 55, and 63% for MO, 2,4-DCP, and 2,4,6-TCP after 90 min of solar irradiation, respectively. The TOC results suggest that the photochemical process in case of MO dye not only undergoes decolorization but also mineralizes the dye solution to a greater extent, whereas the colorless chlorinated phenols are also observed to be mineralized. Thus, it is clear from the figure that not only decolorization but also mineralization takes place during photocatalytic reaction using $ZnIn_2S_4$ flowers as photocatalyst under natural sunlight.

3. CONCLUSIONS

The processing parameters and the precursor concentration play a major role in the development of hexagonal hierarchical $ZnIn_2S_4$ marigold-like flower architectures. The enhancement in the photocatalytic degradation of MO under visible light can be credited to the increase in the dye adsorption due to open cavities in the flower structure facilitating active sites for adsorption and catalysis. The photocatalytic degradation of MO in the system was investigated to be via the superoxide radical that acts as the key active species in the oxidation process. The catalytic activity can be improved by adding hole scavengers to inhibit the recombination of holes and electrons, resulting in more electrons reducing oxygen to superoxide radicals. Complete degradation of both dye and chlorinated phenols was observed within 90 min under natural sunlight irradiation. The catalyst showed efficient recyclability and reusability.

DOI: 10.1021/acsomega.7b01329
ACS Omega 2017, 2, 6926−6938

4. EXPERIMENTAL SECTION

4.1. Synthesis of $ZnIn_2S_4$ Architectures. In a typical synthesis process, stoichiometric ratios of zinc nitrate pentahydrate ($Zn(NO_3)_3{\cdot}5H_2O$) and indium nitrate pentahydrate ($In(NO_3)_3{\cdot}5H_2O$) were dissolved in 30 mL distilled water. A stoichiometric amount of thiourea (CH_4N_2S) was added to the above solution and stirred magnetically to obtain complete dissolution of the compounds. The resulting solution was then transferred to a Teflon-lined beaker having a volume capacity of 60 mL. The capped beaker was put inside a stainless steel autoclave and sealed tightly for hydrothermal treatment at a predetermined temperature in a muffle furnace. After certain time intervals, the autoclave was cooled to room temperature and the precipitate together with the solvent was centrifuged at 5000 rpm to separate the precipitate from the solvent. The precipitate was washed thoroughly with water and absolute ethanol. The centrifuged precipitate was dried at 70 °C for 12 h. The concentration of thiourea played a major role in the formation of crystal phase. Thus, hydrothermal experiments were conducted by varying the ratio of thiourea in the precursor solution. Furthermore, a series of experiments were carried out with varying hydrothermal temperature and time to optimize the crystal structure and morphology. The hydrothermally obtained powders were characterized for their crystallinity, crystal structure, and morphology by different techniques given below.

4.2. Characterizations. Powder X-ray diffraction (XRD) patterns were recorded on Rigaku Miniflex 600 X-ray diffractometer having Cu Kα target with a step size of 0.01 and at the scan rate of 4°/min. Scanning electron microscopic (SEM) imaging was performed using Ultra-55, FESEM Carl Zeiss. TEM samples were prepared by drop casting the dilute ethanolic solution of dispersed photocatalyst on the carbon-coated Cu grid followed by drying in a vacuum desiccator overnight. The specific BET surface areas of the synthesized photocatalysts were measured in a Smart Sorb 92/93 surface area analyzer by nitrogen adsorption/desorption. X-ray photoelectron spectroscopy (XPS) measurements were performed on an ESCA+, Omicron Nanotechnology, Oxford Instruments, Germany, equipped with monochromator Aluminum Source (Al Kα radiation $h\upsilon$ = 1486.7 eV). UV−vis diffuse reflectance spectra were measured using PerkinElmer UV/vis/NIR Lambda 750 spectrophotometer equipped with integrating sphere. Photoluminescence spectra were recorded on LS-55 with 450 W continuous xenon arc lamp as the excitation source and excitation wavelength of 350 nm.

4.3. Photocatalytic Studies. Methyl orange (MO) was taken as a model pollutant to evaluate the photocatalytic property of the optimized photocatalyst. The concentration of the standard stock solution of MO was 20 mg/L. For each of the photocatalytic experiments, catalyst concentration was maintained at 1 g/L. Metal halide lamp (Philips India Ltd.) with λ_{max} around 510 nm was used to perform all of the photodegradation experiments. The lamp was cooled down using the surrounding water jacket connected to the chiller for maintaining the reaction at room temperature. The intensity and the photon flux of the metal halide lamp were determined to be 10^{-7} einstein/s and 220 $\mu W/cm^2$, respectively. The reaction suspension containing catalyst and dye solution was continuously stirred in dark conditions to reach an adsorption−desorption equilibrium. During the catalytic reaction, 2 mL of suspension was taken out at certain time intervals followed by centrifuging at 3000 rpm to separate the catalyst from the dye solution. The absorbance of the clear dye solution was measured by a UV−vis spectrophotometer. The percentage of degradation was calculated as follows: % degradation = $((C_o - C_t)/C_o) \times 100$, where C_o and C_t are the initial (after adsorption) and final absorbance (after photocatalysis) at time t, respectively. Dye solution was also degraded in the presence of light to understand the photolysis process. All of the sunlight experiments were carried out between 12 and 2 p.m., as the fluctuations in solar intensity are minimal in this duration. The variation in solar intensity was recorded using the Eppley PSP 32483F3 radiometer, Newport. The average solar intensity observed was 0.768 kW/m^2. For investigating the active species involved in photodegradation of 20 ppm MO using the optimized catalyst, scavengers were added to the dye solution. The scavengers taken were t-butyl alcohol for hydroxyl radicals ($OH^{\bullet}$), benzoquinone for superoxide radicals ($O_2^{-\bullet}$), glycerol for holes (h^+), and dimethyl sulfoxide for electrons (e^-). The scavenger of 1 mM concentration was added to the reaction solution in the dark reaction (before switching on the light).

Apart from the dye degradation, the catalyst was also used to monitor the degradation of chlorinated phenols, namely, dichlorophenol (2,4-DCP) and trichlorophenol (2,4,6-TCP). However, the standard stock concentration was 50 mg/L. The samples were taken at definite intervals after degradation, and the concentration was determined based on the absorbance at λ_{max} of 280 nm with UV detector using high-performance liquid chromatography (Waters Inc.). C18 column (Poroshell 120) and 50/50 acetonitrile/water with 0.5% formic acid was used as the eluent at a flow rate of 0.4 mL/min.

The total organic carbon (TOC) of both the dye solution and chlorinated phenols at different time intervals of the photochemical reaction was analyzed with the Shimadzu, TOC V_{CSN}analyzer.

AUTHOR INFORMATION

Corresponding Author

*E-mail: adhikari.sangeeta8@gmail.com.

ORCID

Sangeeta Adhikari: 0000-0002-0860-1922

Giridhar Madras: 0000-0003-2211-5055

Author Contributions

†S.A. and A.V.C. contributed equally.

Notes

The authors declare no competing financial interest.

ACKNOWLEDGMENTS

S.A. and A.V.C. would like to thank UGC-Dr. D.S. Kothari Postdoctoral Fellowship scheme, Government of India for research funding. G.M. thanks Department of Science and Technology (DST), India, for J.C. Bose Fellowship. S.A. and A.V.C. also thank Krishna Rao Eswar for FESEM and TEM characterizations.

REFERENCES

(1) Bandala, E. R.; Peláez, M. A.; García-López, A. J.; Salgado, M. d. J.; Moeller, G. Photocatalytic decolourisation of synthetic and real textile wastewater containing benzidine-based azo dyes. *Chem. Eng. Process.* **2008**, *47*, 169−176.

(2) Abe, F. R.; Mendonça, J. N.; Moraes, L. A. B.; de Oliveira, G. A. R.; Gravato, C.; Soares, A. M. V. M.; de Oliveira, D. P. Toxicological

DOI: 10.1021/acsomega.7b01329
ACS Omega 2017, 2, 6926−6938

and behavioral responses as a tool to assess the effects of natural and synthetic dyes on zebrafish early life. *Chemosphere* **2017**, *178*, 282−290.
(3) Guadie, A.; Tizazu, S.; Melese, M.; Guo, W.; Ngo, H. H.; Xia, S. Biodecolorization of textile azo dye using Bacillus sp. strain CH_{12} isolated from alkaline lake. *Biotechnol. Rep.* **2017**, *15*, 92−100.
(4) Lei, P.; Chen, C.; Yang, J.; Ma, W.; Zhao, J.; Zang, L. Degradation of Dye Pollutants by Immobilized Polyoxometalate with H_2O_2 under Visible-Light Irradiation. *Environ. Sci. Technol.* **2005**, *39*, 8466−8474.
(5) Lachheb, H.; Puzenat, E.; Houas, A.; Ksibi, M.; Elaloui, E.; Guillard, C.; Herrmann, J.-M. Photocatalytic degradation of various types of dyes (Alizarin S, Crocein Orange G, Methyl Red, Congo Red, Methylene Blue) in water by UV-irradiated titania. *Appl. Catal., B* **2002**, *39*, 75−90.
(6) Bi, J.; Wu, L.; Li, J.; Li, Z.; Wang, X.; Fu, X. Simple solvothermal routes to synthesize nanocrystalline Bi_2MoO_6 photocatalysts with different morphologies. *Acta Mater.* **2007**, *55*, 4699−4705.
(7) Tang, J.; Zou, Z.; Ye, J. Efficient Photocatalytic Decomposition of Organic Contaminants over $CaBi_2O_4$ under Visible-Light Irradiation. *Angew. Chem., Int. Ed.* **2004**, *43*, 4463−4466.
(8) Maeda, K.; Takata, T.; Hara, M.; Saito, N.; Inoue, Y.; Kobayashi, H.; Domen, K. GaN:ZnO Solid Solution as a Photocatalyst for Visible-Light-Driven Overall Water Splitting. *J. Am. Chem. Soc.* **2005**, *127*, 8286−8287.
(9) Hu, X.; Yu, J. C.; Gong, J.; Li, Q. Rapid Mass Production of Hierarchically Porous $ZnIn_2S_4$ Submicrospheres via a Microwave-Solvothermal Process. *Cryst. Growth Des.* **2007**, *7*, 2444−2448.
(10) Kale, B. B.; Baeg, J.-O.; Lee, S. M.; Chang, H.; Moon, S.-J.; Lee, C. W. $CdIn_2S_4$ Nanotubes and "Marigold" Nanostructures: A Visible-Light Photocatalyst. *Adv. Funct. Mater.* **2006**, *16*, 1349−1354.
(11) Shen, J.; Zai, J.; Yuan, Y.; Qian, X. 3D hierarchical $ZnIn_2S_4$: The preparation and photocatalytic properties on water splitting. *Int. J. Hydrogen Energy* **2012**, *37*, 16986−16993.
(12) Shang, L.; Zhou, C.; Bian, T.; Yu, H.; Wu, L.-Z.; Tung, C.-H.; Zhang, T. Facile synthesis of hierarchical $ZnIn_2S_4$ submicrospheres composed of ultrathin mesoporous nanosheets as a highly efficient visible-light-driven photocatalyst for H_2 production. *J. Mater. Chem. A* **2013**, *1*, 4552−4558.
(13) Han, H.; Riboni, F.; Karlicky, F.; Kment, S.; Goswami, A.; Sudhagar, P.; Yoo, J.; Wang, L.; Tomanec, O.; Petr, M.; Haderka, O.; Terashima, C.; Fujishima, A.; Schmuki, P.; Zboril, R. α-Fe_2O_3/TiO_2 3D hierarchical nanostructures for enhanced photoelectrochemical water splitting. *Nanoscale* **2017**, *9*, 134−142.
(14) Zhang, H. Ultrathin Two-Dimensional Nanomaterials. *ACS Nano* **2015**, *9*, 9451−9469.
(15) Lu, J.; Xie, Y.; Du, G.; Jiang, X.; Zhu, L.; Wang, X.; Qian, Y. "Scission−template−transportation" route to controllably synthesize $CdIn_2S_4$ nanorods. *J. Mater. Chem.* **2002**, *12*, 103−106.
(16) Seo, W.-S.; Otsuka, R.; Okuno, H.; Ohta, M.; Koumoto, K. Thermoelectric properties of sintered polycrystalline $ZnIn_2S_4$. *J. Mater. Res.* **1999**, *14*, 4176−4181.
(17) Romeo, N.; Dallaturca, A.; Braglia, R.; Sberveglieri, G. Charge storage in $ZnIn_2S_4$ single crystals. *Appl. Phys. Lett.* **1973**, *22*, 21−22.
(18) Su, L.; Ye, X.; Meng, S.; Fu, X.; Chen, S. Effect of different solvent on the photocatalytic activity of $ZnIn_2S_4$ for selective oxidation of aromatic alcohols to aromatic aldehydes under visible light irradiation. *Appl. Surf. Sci.* **2016**, *384*, 161−174.
(19) Liu, Q.; Lu, H.; Shi, Z.; Wu, F.; Guo, J.; Deng, K.; Li, L. 2D $ZnIn_2S_4$ Nanosheet/1D TiO_2 Nanorod Heterostructure Arrays for Improved Photoelectrochemical Water Splitting. *ACS Appl. Mater. Interfaces* **2014**, *6*, 17200−17207.
(20) Wang, J.; Chen, Y.; Zhou, W.; Tian, G.; Xiao, Y.; Fu, H.; Fu, H. Cubic quantum dot/hexagonal microsphere $ZnIn_2S_4$ heterophase junctions for exceptional visible-light-driven photocatalytic H_2 evolution. *J. Mater. Chem. A* **2017**, *5*, 8451−8460.
(21) Peng, S.; Li, L.; Wu, Y.; Jia, L.; Tian, L.; Srinivasan, M.; Ramakrishna, S.; Yan, Q.; Mhaisalkar, S. G. Size- and shape-controlled synthesis of $ZnIn_2S_4$ nanocrystals with high photocatalytic performance. *CrystEngComm* **2013**, *15*, 1922−1930.
(22) Joshi, H. M.; Lin, Y. P.; Aslam, M.; Prasad, P. V.; Schultz-Sikma, E. A.; Edelman, R.; Meade, T.; Dravid, V. P. Effects of Shape and Size of Cobalt Ferrite Nanostructures on Their MRI Contrast and Thermal Activation. *J. Phys. Chem. C* **2009**, *113*, 17761−17767.
(23) Zhao, Y.; Frost, R. L.; Martens, W. N. Synthesis and Characterization of Gallium Oxide Nanostructures via a Soft-Chemistry Route. *J. Phys. Chem. C* **2007**, *111*, 16290−16299.
(24) Niederberger, M.; Pinna, N.; Polleux, J.; Antonietti, M. A General Soft-Chemistry Route to Perovskites and Related Materials: Synthesis of $BaTiO_3$, $BaZrO_3$, and $LiNbO_3$ Nanoparticles. *Angew. Chem., Int. Ed.* **2004**, *43*, 2270−2273.
(25) Chaudhari, N. S.; Warule, S. S.; Kale, B. B. Architecture of rose and hollow marigold-like $ZnIn_2S_4$ flowers: structural, optical and photocatalytic study. *RSC Adv.* **2014**, *4*, 12182−12187.
(26) Gou, X.; Cheng, F.; Shi, Y.; Zhang, L.; Peng, S.; Chen, J.; Shen, P. Shape-Controlled Synthesis of Ternary Chalcogenide $ZnIn_2S_4$ and $CuIn(S,Se)_2$ Nano-/Microstructures via Facile Solution Route. *J. Am. Chem. Soc.* **2006**, *128*, 7222−7229.
(27) Shi, L.; Yin, P.; Dai, Y. Synthesis and Photocatalytic Performance of $ZnIn_2S_4$ Nanotubes and Nanowires. *Langmuir* **2013**, *29*, 12818−12822.
(28) Chen, Y.; Huang, R.; Chen, D.; Wang, Y.; Liu, W.; Li, X.; Li, Z. Exploring the Different Photocatalytic Performance for Dye Degradations over Hexagonal $ZnIn_2S_4$ Microspheres and Cubic $ZnIn_2S_4$ Nanoparticles. *ACS Appl. Mater. Interfaces* **2012**, *4*, 2273−2279.
(29) Liu, T.; Wang, L.; Lu, X.; Fan, J.; Cai, X.; Gao, B.; Miao, R.; Wang, J.; Lv, Y. Comparative study of the photocatalytic performance for the degradation of different dyes by $ZnIn_2S_4$: adsorption, active species, and pathways. *RSC Adv.* **2017**, *7*, 12292−12300.
(30) Ahlborg, U. G.; Thunberg, T. M.; Spencer, H. C. Chlorinated Phenols: Occurrence, Toxicity, Metabolism, and Environmental Impact. *Crit. Rev. Toxicol.* **1980**, *7*, 1−35.
(31) Igbinosa, E. O.; Odjadjare, E. E.; Chigor, V. N.; Igbinosa, I. H.; Emoghene, A. O.; Ekhaise, F. O.; Igiehon, N. O.; Idemudia, O. G. Toxicological Profile of Chlorophenols and Their Derivatives in the Environment: The Public Health Perspective. *Sci. World J.* **2013**, *2013*, 1−11.
(32) Batabyal, S. K.; Lu, S. E.; Vittal, J. J. Synthesis, Characterization, and Photocatalytic Properties of In_2S_3, $ZnIn_2S_4$, and $CdIn_2S_4$ Nanocrystals. *Cryst. Growth Des.* **2016**, *16*, 2231−2238.
(33) Tinoco, T.; Polian, A.; Itié, J. P.; López, S. A. Structure of III_a−$ZnIn_2S_4$ under High Pressure. *Phys. Status Solidi B* **1999**, *211*, 385−387.
(34) Sriram, M. A.; McMichael, P. H.; Waghray, A.; Kumta, P. N.; Misture, S.; Wang, X.-L. Chemical synthesis of the high-pressure cubic-spinel phase of $ZnIn_2S_4$. *J. Mater. Sci.* **1998**, *33*, 4333−4339.
(35) Chen, Z.; Li, D.; Zhang, W.; Chen, C.; Li, W.; Sun, M.; He, Y.; Fu, X. Low-Temperature and Template-Free Synthesis of $ZnIn_2S_4$ Microspheres. *Inorg. Chem.* **2008**, *47*, 9766−9772.
(36) Sharma, S. K.; Kushwaha, P. K.; Srivastava, V. K.; Bhatt, S. D.; Jasra, R. V. Effect of Hydrothermal Conditions on Structural and Textural Properties of Synthetic Hydrotalcites of Varying Mg/Al Ratio. *Ind. Eng. Chem. Res.* **2007**, *46*, 4856−4865.
(37) Fang, F.; Chen, L.; Chen, Y.-B.; Wu, L.-M. Synthesis and Photocatalysis of $ZnIn_2S_4$ Nano/Micropeony. *J. Phys. Chem. C* **2010**, *114*, 2393−2397.
(38) Chen, W.; Liu, T.-Y.; Huang, T.; Liu, X.-H.; Duan, G.-R.; Yang, X.-J.; Chen, S.-M. A novel yet simple strategy to fabricate visible light responsive C,N-TiO_2/g-C_3N_4 heterostructures with significantly enhanced photocatalytic hydrogen generation. *RSC Adv.* **2015**, *5*, 101214−101220.
(39) Li, M.; Su, J.; Guo, L. Preparation and characterization of $ZnIn_2S_4$ thin films deposited by spray pyrolysis for hydrogen production. *Int. J. Hydrogen Energy* **2008**, *33*, 2891−2896.
(40) Chen, Y.; Tian, G.; Zhou, W.; Xiao, Y.; Wang, J.; Zhang, X.; Fu, H. Enhanced photogenerated carrier separation in CdS quantum dot sensitized $ZnFe_2O_4/ZnIn_2S_4$ nanosheet stereoscopic films for excep-

DOI: 10.1021/acsomega.7b01329
ACS Omega 2017, 2, 6926−6938

tional visible light photocatalytic H_2 evolution performance. *Nanoscale* **2017**, *9*, 5912−5921.
(41) Li, H.; Yu, H.; Chen, S.; Zhao, H.; Zhang, Y.; Quan, X. Fabrication of graphene wrapped $ZnIn_2S_4$ microspheres heterojunction with enhanced interfacial contact and its improved photocatalytic performance. *Dalton Trans.* **2014**, *43*, 2888−2894.
(42) Ye, L.; Fu, J.; Xu, Z.; Yuan, R.; Li, Z. Facile One-Pot Solvothermal Method to Synthesize Sheet-on-Sheet Reduced Graphene Oxide (RGO)/$ZnIn_2S_4$ Nanocomposites with Superior Photocatalytic Performance. *ACS Appl. Mater. Interfaces* **2014**, *6*, 3483−3490.
(43) Zhou, J.; Tian, G.; Chen, Y.; Meng, X.; Shi, Y.; Cao, X.; Pan, K.; Fu, H. In situ controlled growth of $ZnIn_2S_4$ nanosheets on reduced graphene oxide for enhanced photocatalytic hydrogen production performance. *Chem. Commun.* **2013**, *49*, 2237−2239.
(44) Cai, W.; Zhao, Y.; Hu, J.; Zhong, J.; Xiang, W. Solvothermal Synthesis and Characterization of Zinc Indium Sulfide Microspheres. *J. Mater. Sci. Technol.* **2011**, *27*, 559−562.
(45) Mai, F. D.; Lu, C. S.; Wu, C. W.; Huang, C. H.; Chen, J. Y.; Chen, C. C. Mechanisms of photocatalytic degradation of Victoria Blue R using nano-TiO_2. *Sep. Purif. Technol.* **2008**, *62*, 423−436.
(46) Yang, J.; Dai, J.; Chen, C.; Zhao, J. Effects of hydroxyl radicals and oxygen species on the 4-chlorophenol degradation by photoelectrocatalytic reactions with TiO_2-film electrodes. *J. Photochem. Photobiol., A* **2009**, *208*, 66−77.
(47) Chen, Z.; Li, D.; Zhang, W.; Shao, Y.; Chen, T.; Sun, M.; Fu, X. Photocatalytic Degradation of Dyes by $ZnIn_2S_4$ Microspheres under Visible Light Irradiation. *J. Phys. Chem. C* **2009**, *113*, 4433−4440.
(48) Chen, Y.; Hu, S.; Liu, W.; Chen, X.; Wu, L.; Wang, X.; Liu, P.; Li, Z. Controlled syntheses of cubic and hexagonal $ZnIn_2S_4$ nanostructures with different visible-light photocatalytic performance. *Dalton Trans.* **2011**, *40*, 2607−2613.
(49) Shiragami, T.; Shimizu, Y.; Hinoue, K.; Fueta, Y.; Nobuhara, K.; Akazaki, I.; Yasuda, M. Silica gel-supported porphyrinatoantimony(V) complex acting as visible-light driven photocatalyst for dechlorination of chlorophenols in aqueous solution. *J. Photochem. Photobiol., A* **2003**, *156*, 115−119.
(50) Chen, Y.-C.; Smirniotis, P. Enhancement of Photocatalytic Degradation of Phenol and Chlorophenols by Ultrasound. *Ind. Eng. Chem. Res.* **2002**, *41*, 5958−5965.
(51) Chung, S.-G.; Chang, Y.-S.; Choi, J.-W.; Baek, K.-Y.; Hong, S.-W.; Yun, S.-T.; Lee, S.-H. Photocatalytic degradation of chlorophenols using star block copolymers: Removal efficiency, by-products and toxicity of catalyst. *Chem. Eng. J.* **2013**, *215*−*216*, 921−928.

DOI: 10.1021/acsomega.7b01329
ACS Omega 2017, 2, 6926−6938